Materials Today Chemistry 23 (2022) 100668

Contents lists available at ScienceDirect

Materials Today Chemistry

journal homepage: www.journals.elsevier.com/materials-today-chemistry/

Alkaline oxygen evolution: exploring synergy between *fcc* and *hcp* cobalt nanoparticles entrapped in N-doped graphene

Ajit Kumar Singh [a, f], Seulgi Ji [b, f], Baghendra Singh [a], Chittaranjan Das [c], Heechae Choi [b, ***], Prashanth W. Menezes [d, e, **], Arindam Indra [a, *]

[a] Department of Chemistry, IIT (BHU), Varanasi, UP 221005, India
[b] Theoretical Materials & Chemistry Group, Institute of Inorganic Chemistry, University of Cologne, Greinstr. 6, 50939 Cologne, Germany
[c] Applied Physics and Sensors, Brandenburg University of Technology, Cottbus, Konrad Wachsmann Allee 17, 03046 Cottbus, Germany
[d] Metalorganics and Inorganic Materials, Department of Chemistry, Technische Universität Berlin, Straße des 17 Juni 135, Sekr. C2, 10623 Berlin, Germany
[e] Materials Chemistry Group for Thin Film Catalysis – CatLab, Helmholtz-Zentrum Berlin für Materialien und Energie, Albert-Einstein-Str. 15, 12489 Berlin, Germany

ARTICLE INFO

Article history:
Received 26 July 2021
Received in revised form
21 September 2021
Accepted 1 November 2021
Available online xxx

Keywords:
Co nanoparticles
Nitrogen doped graphene
Core-shell structure
Phase effect
Water oxidation

ABSTRACT

Herein, we report a Mott-Schottky catalyst by entrapping cobalt nanoparticles inside the N-doped graphene shell (Co@NC). The Co@NC delivered excellent oxygen evolution activity with an overpotential of merely 248 mV at a current density of 10 mA cm^{-2} with promising long-term stability. The importance of Co encapsulated in NC has further been demonstrated by synthesizing Co nanoparticles without NC shell. The synergy between the hexagonal close-packed (*hcp*) and face-centered cubic (*fcc*) Co plays a major role to improve the OER activity, whereas the NC shell optimizes the electronic structure, improves the electron conductivity, and offers a large number of active sites in Co@NC. The density functional theory calculations have revealed that the *hcp* Co has a dominant role in the surface reaction of electrocatalytic oxygen evolution, whereas the *fcc* phase induces the built-in electric field at the interfaces with N-doped graphene to accelerate the H^+ ion transport.

1. Introduction

Electrochemical energy conversion using earth-abundant materials with high activity and long-term stability is one of the key features for renewable and clean energy production [1–4]. The anodic oxygen evolution reaction (OER) is a counterpart to the hydrogen evolution reaction (HER) in an electrochemical water splitting cell [1–4]. The OER ($4OH^- \rightarrow O_2 + 2H_2O + 4e^-$) involves the transfer of multiple protons and electrons and is both thermodynamically and kinetically demanding [1–4]. Although noble metal oxides (RuO_2, IrO_2) have been considered as the state-of-the-art catalysts for OER, the lack of stability, high cost, and low abundance of the noble metal-based catalysts restrict their large-scale applications [5–7]. Therefore, tremendous efforts have been made to develop efficient OER catalysts with earth-abundant transition metals [5–11].

Among various synthetic strategies developed for catalyst design, the modulation of the electronic structure of the active sites and optimization of the binding energy of the reaction intermediates have been found to be effective to promote catalytic activity [12]. In this respect, designing the Mott-Schottky electrocatalyst by forming N-doped graphene (NC) shell on the surface of the catalyst nanoparticles (NPs) is highly promising [13,14]. The role of the NC layer in the heterogeneous catalyst is similar to the ligand(s) in the homogeneous system [15]. As the Schottky barrier is continuous, the semiconducting NC heterojunction, formed on the surface of the NPs, can control the electron density within the catalyst by adjusting the Fermi level charge flow through the interface [16]. Recently, the concept of Mott-Schottky catalysts has been established in water splitting and in various catalytic organic reactions [12,13,17,18].

Within the active electrocatalysts, N-doped carbon-based materials with an adjustable electron structure have been found to be

* Corresponding author.
** Corresponding author.
*** Corresponding author.
E-mail addresses: h.choi@uni-koeln.de (H. Choi), prashanth.menezes@mailbox.tu-berlin.de, prashanth.menezes@helmholtz-berlin.de (P.W. Menezes), arindam.chy@iitbhu.ac.in (A. Indra).
[f] These authors contributed equally to this article.

https://doi.org/10.1016/j.mtchem.2021.100668
2468-5194/

beneficial to promote the electrochemical activity of various nanocatalysts [19–25]. Mostly, metal-organic framework (MOF)-derived M@NC- and MX_n@NC- (M = transition metal, X = P, S, Se, etc. and n > 0) type catalysts have been explored for the cathodic HER [19,20, 26-32]. For example, zeolitic imidazolate framework- and Prussian blue analog–derived catalysts such as alloys [26,30], phosphides [27,32], and chalcogenides [28] with core-shell structures containing N-doped carbon shell have been reported with excellent electrochemical HER performances. The superior catalytic activity and durability of M@NC for HER have been ascribed to the faster electron transfer kinetics from N-doped carbon shell to metal core, the presence of M–N–C active sites, and protective NC shells as well as the stronger binding ability of NC and the adsorbates [33].

In contrast to HER, the NC shell on the catalyst surface is inactive for OER and reduces the number of active sites by hindering overall efficiency [34]. As a result, carbon-rich materials require a much higher overpotential for anodic OER [34]. Therefore, an optimization of the catalyst structure by controlling the thickness of the NC layer is required to avail of high OER activity. Interestingly, the metal-rich catalyst with ultrathin NC shell could be the ideal choice to promote OER processes [35,36]. For example, catalysts such as Co@NC [37], Co–N–C [38], and Co–NC/CNT [39] were explored for the electrochemical OER where the variation in the N/C ratio, nature of nitrogen (pyridinic, pyrollic, etc.), and thickness of the NC layer led to a wide variation in the electrocatalytic activity. However, the distribution of the Co NPs in these catalysts is not uniform. In addition, the Co NPs with varying sizes and a different number of NC layers are embedded in the carbon (or N-doped carbon) matrix [37–39]. As a result, the catalyst system became highly complex, and the effect of NC layers on the OER activity was difficult to realize. Therefore, designing of Co@NC system with a defined particle size and an optimum number of NC layers is still a challenge. Moreover, a direct comparison of the OER activities of bare Co NPs and Co@NC has not been previously explored to elucidate the essential role of the NC layer on the surface. These lacunae in this field led us to design Co@NC catalyst having Co NPs with uniform size and a defined number of N-doped graphene layers on the surface. Furthermore, we explored the effect of the NC layer on Co NPs by comparing their OER activities. The difference in the activities was also explained by electrochemical, spectroscopic, microscopic, and DFT studies.

It should be mentioned here that previously cobalt-based NPs with *fcc* phase have been explored for water oxidation in alkaline medium [33,40]. However, the effect of different phases of the metal on the catalytic OER activity was rarely studied. Recently, superior OER performance of *hcp* Ni over *fcc* phase has been demonstrated by Wang et al. [41]. However, the reason behind the difference in the OER activity with different phases of metal was never described. Herein, we present a facile strategy for the synthesis of a Mott-Schottky electrocatalyst by introducing an N-doped graphene shell on the surface of the cobalt nanoparticles (Co@NC) containing the mixture of *fcc* and *hcp* phases and explain the synergy between the two phases with the NC shell to improve the OER activity.

A complex Co-NTA (NTA = nitrilotriacetic acid) has been used as the precursor for the formation of Co@NC by low-temperature pyrolysis (Scheme 1). The importance of the N-doped graphene shell has further been established by the superior electrochemical performance of Co@NC over Co NPs in an alkaline electrolyte. The Co@NC produced only an overpotential 248 mV at a geometric current density of 10 mA/cm^2, whereas an overpotential of 290 mV was required for Co NPs to reach the same current density. In addition, Co@NC generated constant current for OER under chronoamperometric conditions. Most notably, the DFT calculations have shown the synergy between *fcc* and *hcp* Co nanoparticles to improve the H^+ ion transport and to facilitate the surface reactions during water oxidation, respectively.

2. Results and discussions

The catalyst precursor Co-NTA was prepared by the hydrothermal reaction of cobalt chloride and nitrilotriacetic acid (see experimental) [42]. The precursor was characterized by powder X-ray diffraction (PXRD; Fig. S1) [42]. Infrared spectra showed the vibrations corresponding to carbonyl functions (Fig. S2) [42]. The nanorod morphology of Co-NTA was revealed by scanning electron microscopic (SEM; Fig. S3) and transmission electron microscopic (TEM; Fig. S4) studies.

Pyrolysis of Co-NTA in an argon atmosphere at 500°C produced Co@NC (see experimental) [42]. Notably, the temperature used for the synthesis of Co@NC was significantly lower compared with the temperature (~900°C) reported for M@NC catalysts prepared from MOFs [43]. The reflections in the PXRD pattern further confirmed the only presence of metallic Co and was a mixture of hexagonal (JCPDS card no. 05-0727) and cubic (JCPDS card no. 15-0806) phases (Fig. S5) [44,45]. The co-existence of Co in two different crystal forms, hexagonal and cubic, has also been reported previously [46]. The average crystallite size was calculated using the Scherrer equation and found to be 23 nm, which is in good agreement with the TEM data (see later). In addition to this, a broad peak for graphitic carbon (002) was detected at a two-theta value of 24° [46]. The elemental analysis of Co@NC confirmed N-doping in carbon (13.6% of carbon and 1.7% of nitrogen).

SEM studies of Co@NC showed spherical nanoparticles assembled together with carbon nanofiber to form one-dimensional growth of the nanostructures (Fig. 1a and S6). TEM analysis of Co@NC also confirmed that the assembly of spherical nanoparticles and carbon nanofibers (Fig. 1b). The selected area electron diffraction (SAED) pattern revealed the crystalline nature of the core (Fig. 1b, inset). The core-shell structure of the spherical nanoparticles with a Co core wrapped within an N-doped graphene shell was revealed by high-resolution TEM (HRTEM). The diameter of the core was determined to be 27 nm, whereas the thickness of the N-doped graphene shell was detected to be 2–3 nm (Fig. 1c). The shell

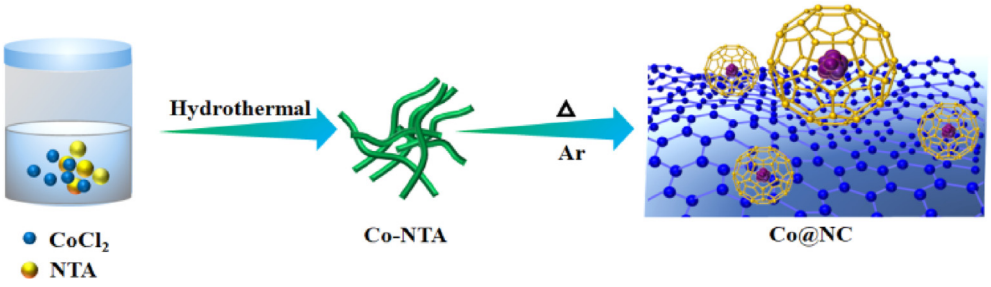

Scheme 1. Schematic representation for the synthesis of the Mott-Schottky electrocatalyst Co@NC from the precursor complex Co-NTA.

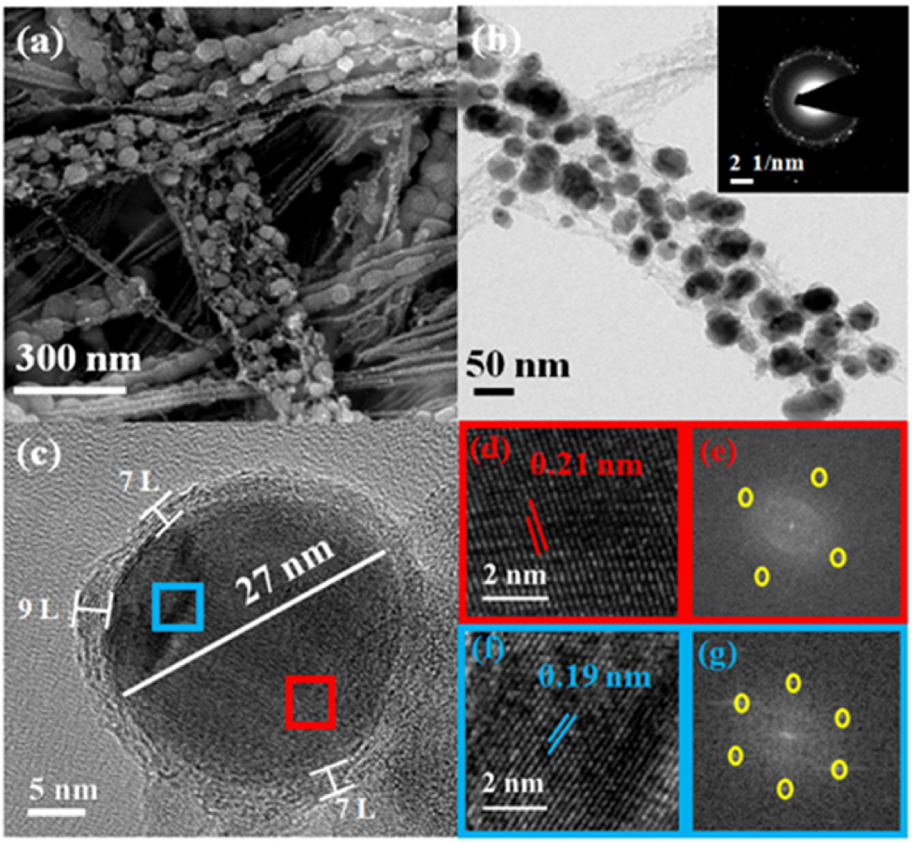

Fig. 1. (a) SEM image of Co@NC showing the assembly of the spherical nanoparticles to form the nanostructures. (b) TEM image of Co@NC and inset showing the SAED pattern. (c) HRTEM image of a Co@NC nanoparticle exhibiting the core (diameter 27 nm) and N-doped graphene shell with 7–9 graphene layers (thickness 2–3 nm). (d) The d-spacing of 0.21 nm corresponding to the (111) plane of the cubic cobalt (*Fm3m*) and (e) corresponding FFT pattern. (f) The d-spacing of 0.19 nm corresponding to the (220) plane of the hexagonal cobalt (space group: *P63/mmc*) and (g) corresponding FFT pattern.

consisted of seven to nine layers of N-doped graphene with a d-spacing of 0.34 nm corresponding to the (002) plane of graphene [44–46]. It was observed that the core was a combination of the cubic (space group: *Fm*3*m*) and hexagonal (space group: *P*6$_3$/*mmc*) cobalt formed by the favorable co-crystallization (Fig. 1d and f) [46]. Fast Fourier transfer (FFT) pattern of HRTEM images also proved the presence of cubic and hexagonal cobalt in Co@NC (Fig. 1e and g) [46]. Energy dispersive X-ray (EDX) spectra exhibited the presence of Co, C, and N in Co@NC, whereas EDX mapping showed the distribution of the elements (Fig. S7).

Information about the nature of the N-doped graphene shell was deduced from the Raman spectroscopic studies of the powder Co@NC sample (Fig. S8). The Raman spectrum of Co@NC displayed three peaks at 1349, 1590, and 2700 cm^{-1} representing D, G, and 2D bands, respectively [47,48]. The intensity ratio of D and G bands (I_D/I_G) was calculated to be 1.19, signifying a large number of defects in the graphitic carbon layers due to the N-doping. The comparatively broad second-order band (2D) and 2D/G peak intensity ratio (1.88) also indicates that the shell is made of thin graphene with few layers [49]. Furthermore, the Tuinstra–Koenig equation (see the experimental part) was used to determine the crystalline size. The size of the Co@NC was calculated to be 14.08 nm [50].

The electronic environment and oxidation states of the elements in Co@NC were determined by X-ray photoelectron spectroscopy (XPS) studies. High-resolution Co 2p spectrum showed two peaks at 779.2 eV and 795.0 eV corresponding to Co 2p$_{3/2}$ and Co 2p$_{1/2}$ (Fig. S9) [51,52]. The deconvolution of the Co 2p$_{3/2}$ peak revealed the presence of Co^0 (778.5 eV) and Co–N (781.8 eV) species [51–53]. The peaks at 780.4 eV and 779.6 eV indicated the existence of Co(II) and Co(III) species, originated from the surface oxidation of cobalt nanoparticles [54]. The corresponding satellite peak of Co(II) was detected at a binding energy of 786.4 eV (Fig. S9). The Co 2p XPS spectrum also showed the electron transfer from the NC shell to the Co species (Co (0) = 778.1 eV), indicating a strong electronic interaction [55].

N 1s XP-spectrum was deconvoluted into five peaks for Co–N bonding, pyridinic-N, pyrrolic-N, graphitic-N, and oxidized-N species (Fig. S10) [51–54]. The C 1s XPS spectrum was fitted for C–C and C=O and C–N bonds (Fig. S11) [56]. The four peaks in the O 1s spectrum were attributed to C=O, C–OH, C–C=O, and C–O–C species (Fig. S12) [56–58].

To demonstrate the advantages of the N-doped graphene shell on the Co nanoparticles in Co@NC, we additionally synthesized Co NPs with identical structure and morphology (see experimental in SI) [59]. The as-synthesized Co NPs were well characterized by the state-of-the-art techniques, and the related discussions are provided in Fig. S13, Fig. S14, and Fig. S15.

The catalysts Co@NC and Co NPs were deposited on Ni foam (NF) by an electrophoretic deposition (EPD) method (see experimental). Subsequently, the water oxidation activities of the catalysts were performed in 1.0 M aqueous KOH solution using linear sweep voltammetry (LSV; Fig. 2) with a three-electrode set up. The current density of Co@NC/NF started to increase at an applied potential of 1.45 vs. reversible hydrogen electrode (RHE) and reached 400 mA/cm^2 at 1.64 vs. RHE, whereas the Co NPs displayed substantially lower catalytic activity. Cyclic voltammetric (CV) studies were performed to understand the activation of Co@NC under anodic potential (Fig. S16). The anodic activation of

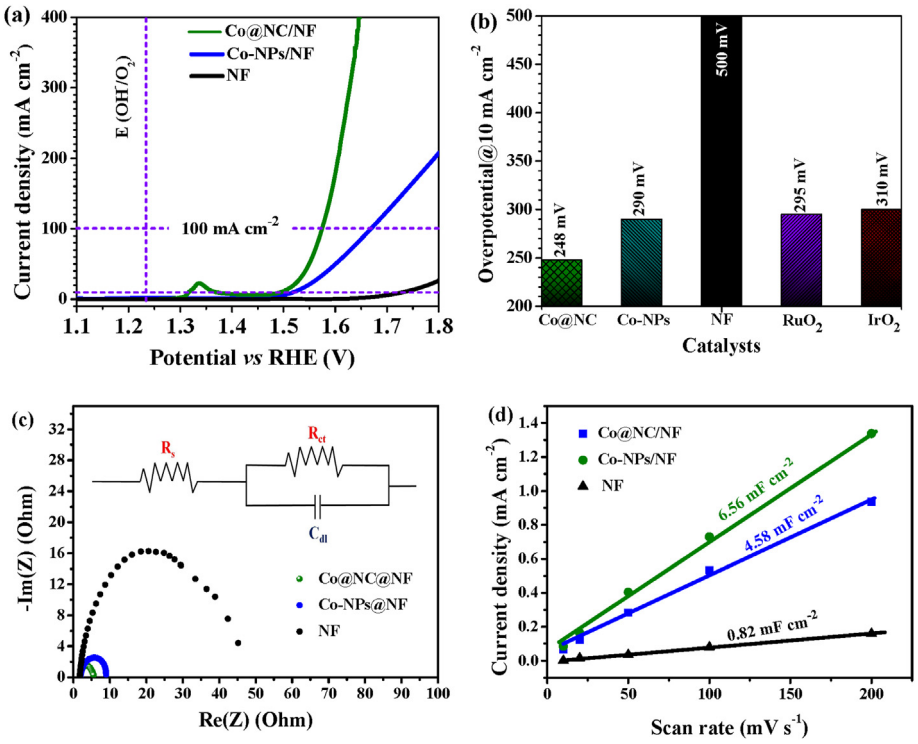

Fig. 2. (a) LSV profiles for OER (scan rate 1 mV/s), (b) bar diagram representing a comparison of the overpotentials (including noble catalysts); (c) Nyquist plot, (d) comparison of the C_{dl} of Co@NC/NF, Co NPs/NF, and NF in 1.0 M aqueous KOH solution.

Co@NC led to an improvement in the OER activity with increasing number of CV cycles (50 cycles; Fig. S16a). The CV profile clearly shows two pre-peaks—A_1 for the oxidation of Co^{2+} to Co^{3+} (1.33 V vs. RHE) and A_2 for the oxidation Co^{3+} to Co^{4+} (1.42 V vs. RHE; Fig. S16b) [60]. This anodic activation of Co@NC resulted in the formation of active catalyst cobalt (oxy)hydroxide@NC (see later) [61,62].

The OER overpotential needed to reach a current density of 10, and 100 mA/cm^2 for Co@NC was merely 248 and 340 mV, whereas an overpotential 290 and 430 mV was required for Co NPs to attain the same current density (Fig. 2a). The bare NF (prepared in the same EPD condition) was inactive for OER. The poor performance of Co NPs in comparison to Co@NC clearly established the importance of Mott-Schottky catalyst for enhanced electrochemical performance (Fig. 2b). In addition, the obtained overpotential for Co@NC is better than the commercially available noble metal catalysts RuO_2, IrO_2, Pt (Fig. 2b and S17), and other non-noble metal-based catalysts reported in the literature on Ni foam support (Table S1).

To further assess the reaction kinetics of the catalysts, Tafel plots were constructed from LSV curves that showed a Tafel slope of 50 mV/dec for Co@NC and 113 mV/dec for Co NPs (Fig. S18). As the electrochemical long-term stability is a key criterion for practical applications, the Co@NC catalyst was investigated by chronoamperometric (CA) measurements at an overpotential of 260 mV that exhibited stable current density over 48 h (Fig. S19). In the CA profile, an increment in the current density was observed for the first 23 h, indicating the activation of Co@NC to the active catalyst Co(O)OH@NC. After that, the catalyst produced a stable current up to 48 h. The CV profile after 48 h CA measurements also confirmed the long-term stability of the catalyst under harsh electrochemical water oxidation conditions (Fig. S20). The efficiency of Co@NC for the water oxidation was further confirmed by achieving 95% Faradaic efficiency (Table S2). The turnover frequency (TOF) for Co@NC was determined at 100 mA/cm^2 current density and calculated to be 2.15 per second.

The factors associated with the catalytic kinetics and interfacial properties for the enhanced electrochemical performance of Co@NC were evaluated by the electrochemical impedance measurements. The Nyquist plot revealed the lowest semicircle radius for the Co@NC compared with the Co NPs and NF (Fig. 2c). The lowest charge transfer resistance (R_{ct}) value was determined for Co@NC (3.87 Ω) compared with the Co nanoparticles (7.27 Ω) and NF (43.517 Ω). This indicated the lowest charge transfer resistance of Co@NC providing improved electronic conductivity. The electrochemically active surface area (ECSA) of the investigated catalysts was determined from electrochemical double-layer capacitance (C_{dl}), which is expected to be linearly proportional to the ECSA. The C_{dl} was evaluated by measuring the non-Faradic capacitive currents related to double-layer charging from the scan rate dependence of CVs (Fig. S21). A C_{dl} of 6.56 mF/cm^2 was determined for Co@NC, larger than that of Co NPs (4.58 mF/cm^2) and bare NF (0.82 mF/cm^2; Fig. 2d). This result demonstrated the presence of rich catalytically active surface sites in Co@NC compared with the Co NPs.

To gain insights into the chemical and the electronic structure of Co@NC during alkaline OER, XPS and TEM analyses were carried out after 48 h of CA (CA-OER) measurements. After CA-OER, The Co 2p XPS spectrum of Co@NC showed two peaks at 779.1 and 794.7 eV, assigned for Co $2p_{3/2}$ and Co $2p_{1/2}$, respectively (Fig. S22) [51–54]. The Co $2p_{3/2}$ deconvoluted peaks at 778.9 eV and 780.3 eV were assigned for Co(III) and Co(II) species, respectively. The spin-orbit spacing for $Co2p_{3/2}$–$Co2p_{1/2}$ was calculated to be 15.4 eV [63]. This result indicates the presence of a high amount of Co(III) in the active catalyst structure formed by the anodic oxidation of the metallic Co during OER.

The O 1s spectrum of Co@NC after CA-OER was fitted into three peaks at 529.5 eV, 530.4 eV, and 531.5 eV (Fig. S23) [64,65]. Two

distinct peaks for Co–O bond (529.5 eV) and Co–OH bond (530.4 eV) were appeared because of the formation of Co(O)OH@NC by the anodic oxidation of Co@NC in the alkaline medium, and the third peak at 531.5 eV indicated the hydration of the catalyst during activation of the catalyst [64,65].

The N 1s XP-spectrum was fitted into two peaks at 398.5 eV and 400.2 eV that indicated the presence of pyridinic-N and pyrrolic-N (Fig. S24) [51–54]. The C 1s XPS spectrum showed the peaks for 284.5 eV (C–C), 285.4 eV (C–O), 287.9 eV (C=O), 291.2 eV (O–C–OH), and 292.6 eV (O–C=O) (Fig. S25) [66]. From the C 1s spectrum, it was confirmed that carbon was more oxidized after CA compared with the fresh catalyst.

TEM images disclosed a slight agglomeration of the Co@NC particles after CA-OER measurements (Fig. S26). HRTEM studies specified that the N-doped graphene layer on the surface of the Co nanoparticles remained intact. The existence of the N-doped graphene layer was confirmed from HRTEM, which detected the lattice spacing of 0.34 nm, indexed for the (002) plane of graphitic carbon shell [44–46]. The lattice spacing of 0.21 nm was detected in the core corresponding to the (200) plane of Co(O)OH (JCPDS card no. 26-480) [67]. This result also revealed that the inner cobalt core was oxidized from Co(0) to Co(II)/Co(III) to form Co(O)OH active catalyst structure as supported by XPS data.

The major advantages associated with Co@NC arise from the N-doped graphene layer on the surface of the cobalt nanoparticles. Although the core (cobalt nanoparticle) is not stable under alkaline water oxidation and undergoes electrochemical activation to form Co(O)OH@NC as the active catalyst, the NC layer on the surface remains intact. The NC layer acts as the sink of electrons and controls the electron flow during water oxidation [15,16]. As a result, a significant improvement in the OER activity was observed for Co@NC compared with bare Co NPs. Even the OER activity of Co@NC was observed to be superior to many other cobalt-based catalysts reported in the literature (Table S1). In addition, the NC layer protects the complete agglomeration of the Co NPs so that the nanoparticles can retain their morphology even after long-term oxygen evolution. This indeed significantly improves the stability of the catalyst system.

To understand the difference in the oxygen evolution activity of Co and Co@NC and the effect of the cubic and hexagonal phases of Co in OER, DFT calculations were carried out. Based on the OER reaction steps (Scheme S1), we calculated the Gibbs free energies of OH, O, and OOH on Co(*fcc*)@NC, Co(*fcc*)@C, Co(*hcp*)@NC, and Co(*hcp*)@C (see calculation method in SI). The fully relaxed atomic structures of OER intermediates (OH, O, OOH) adsorbed Co@C slab models showed all-downhill energy steps in OER (Fig. 3). At pH 14, both Co(*hcp*)@NC(py) (py = pyridinic-N) and Co(*hcp*)@NC(pyr) (pyr = pyrrolic-N) showed free energy downhill, whereas Co(*hcp*)@C revealed energy uphill with a tiny barrier, close to the thermal energy at room temperature (0.03 eV). Therefore, Co(*hcp*)@C has favorable surface reaction kinetics for OER under alkaline conditions.

Co(*fcc*), Co(*fcc*)@NC(pyr), and Co(*fcc*)@C have very high energy barriers (Fig. 3), and only Co(*fcc*)@NC(py) was predicted to have high surface reaction kinetics as shown in the energy landscapes (Fig. 3). Therefore, the overall OER activity of Co(*fcc*)@C is low because of the high energy barriers in the reaction step of OOH formation of Co(*fcc*)@NC(pyr) and Co(*fcc*)@C. As selective production of pyrrolic-N and pyridinic-N is difficult, Co(*fcc*)@NC cannot be considered as a good OER catalyst, no matter how good is a pyridinic phase of Co(*fcc*)@NC in OER. Therefore, the synergistic effect of the mixed-phase Co cannot be explained only by surface reaction energy landscapes.

As electrical conductivity is also one of the key factors for catalytic activities, we calculated the electron density of states (DOS) to compare the electron populations at Fermi energy of Co(*hcp*) and Co(*fcc*) in the interface of C and NC (Fig. S27) [68]. The total DOS of all the phases showed high electron state populations near the Fermi energy level, which indicates that the metallicities of Co(*hcp*) and Co(*fcc*) are well preserved when entrapped inside C and NC shell. However, it showed that the conductivity of all the systems was not significantly changed regardless of Co phases and the type of N-doping. This is in good agreement with the experimental results.

The Co(*hcp*)@NC, Co(*hcp*)@C has nearly zero electric fields near the graphene surfaces, indicating that there are weak driving forces to transport H^+ ions. On the other hand, Co(*fcc*)@C and Co(*fcc*)@NC showed finite positive values of electric field, 0.08V/Å and 0.11V/Å (Fig. 4). Therefore, the existence of *fcc* phase Co provides strong driving forces to transport H^+ ions and prevents the local pH reduction. Compared with the electric field strength of Co(*fcc*)@C, that of Co(*fcc*)@NC notably increased by 35%. H^+ ions generated by OER can be thereby further accelerated by the interface electric field of Co(*fcc*)@NC. Hence, Co(*fcc*)@NC can play an important role in prompting H^+ ions transport away from the carbon surface. Our theoretical analyses well explain the synergistic impacts of *hcp* and *fcc* phase Co in Co@NC in the OER: each phase has a different role. Previously different OER activities of the *fcc* and *hcp* phases of Ni have been demonstrated, but no effort has been made to understand the experimental results [41]. The present work confirmed that multiphase metallic particles in metal-N-doped graphene heterogeneous catalyst can have high catalytic activities being well designed with considerations of the different roles of the phases.

As four protons and four electrons are involved in the overall process of OER, H^+(aq) ions should be removed from the catalytic surface to attain better activity [69]. The H^+ ion transport efficiency

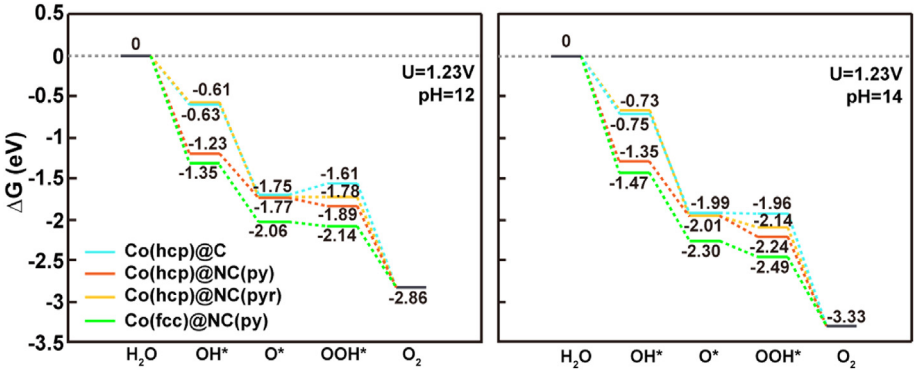

Fig. 3. Calculated free energy diagram of the intermediates in OER on four Co-graphene/N-doped graphene systems with U = 1.23 V at pH 12 (left) and 14 (right).

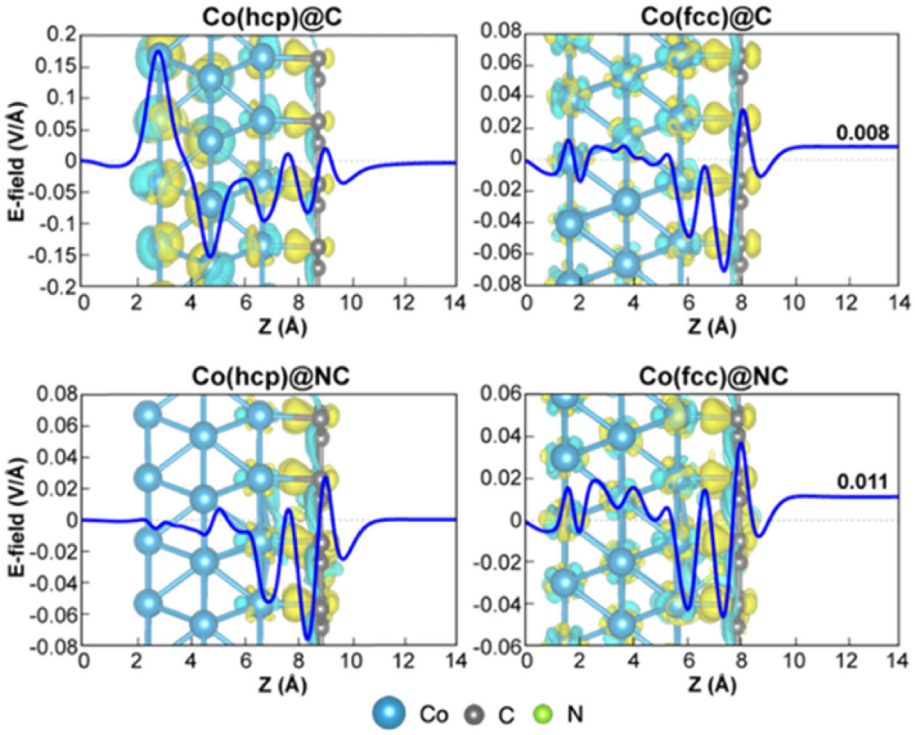

Fig. 4. The yellow and blue regions represent the electron accumulation and depletion regions, respectively. The isovalue is set at 0.03 e/Bohr. The sky blue, black, green, red, and pink balls indicate Co, C, N, O, and H atoms, respectively. N, O and H atoms are not visible in this direction of the figure.

mostly relies only on diffusion, a relatively weak driving force for H^+ mobility, and leads to significant local pH reduction [70,71]. We assumed that the improved OER activity of Co@NC was originated from the mixed Co phases (*hcp* and *fcc*), an additional driving force to keep H^+ ion concentration low near the catalyst surface (Fig. 4). Previous studies on metal-graphene heterostructures have also shown a significant amount of charge transfer between metal particles and graphene layers, inducing large dipole moments (Equations S2-S5) [72,73].

3. Conclusions

In conclusion, we have demonstrated a controlled synthesis of a Mott-Schottky catalyst, Co@NC, where Co nanoparticles are entrapped inside a thin N-doped graphene shell. The Co@NC displayed strikingly better OER overpotentials, Tafel slope, ECSA, charge transfer resistance, and long-term stability than that of Co NPs. The N-doped graphene shell significantly improves the adsorption of the reaction intermediates on the surface of the active catalyst and fastens the reaction kinetics of OER. In addition, the synergy of the *hcp* and *fcc* phases of Co plays a crucial role to improve the OER activity. The *hcp* phase of Co controls the surface reaction of electrocatalytic oxygen evolution, and the *fcc* phase induces the built-in electric field at the interfaces with N-doped graphene to accelerate the H^+ ion transport. The presented work provides a new facile strategy to design active non-noble metal-based OER electrocatalysts in a controlled way that may find great potential for water electrolysis, oxygen reduction reaction, and rechargeable batteries.

4. Experimental section

Synthesis of Co-NTA: 6 mmol of $CoCl_2.6H_2O$ was dissolved in 15 mL of double distilled water and stirred for 30 min to make a homogeneous solution [74]. 3 mmol of NTA was dispersed in 15 mL of isopropanol and stirred for 30 min. NTA dispersion was added to the cobalt chloride solution and stirred for 30 min. The obtained suspension was transferred into a Teflon-coated autoclave (50 mL volume) and placed it in a preheated oven (180°C) for 6 h. The autoclave was allowed to come down to room temperature by natural cooling. The pink color precipitate was collected, washed with double distilled water five times, and finally with ethanol by centrifugation at 8,000 rpm for 10 min. Collected solid was dried in a hot air oven at 60 °C for 6 h.

Synthesis of Co@NC: The fine powder of Co-NTA (100 mg) was placed in a crucible boat and pyrolyzed at 500°C in the Ar atmosphere for 2 h (in a tubular furnace with heating rate: 2 °C/min) [42]. The furnace was allowed to naturally cool down to room temperature. The black powder was collected and denoted as Co@NC.

Synthesis of Co NC:A mixture of polyethylene glycol (PEG 4000, 2 g), $CoCl_2.6H_2O$ (0.24 g), and ethylene glycol (100 mL) was heated at 150°C under inert (N_2) atmosphere with vigorous stirring to get a clear solution [59]. The temperature of the solution was increased to 170°C, and a suspension of $NaBH_4$ (0.7 g) in ethanol (10 mL) was added to the solution over a period of 20 min. The reflux was continued for 30 min after the complete addition of $NaBH_4$. The reaction mixture was cooled down to room temperature. The Co NPs were collected by centrifugation (10,000 rpm) and washed thoroughly with ethanol and dried overnight at 50°C.

Characterization:PXRD was recorded in Bruker AXS D8 advanced diffractometer equipped with a position-sensitive detector and curved germanium (111) primary monochromator. The radiation used was Cu-$K\alpha$ ($\lambda = 1.5418$ Å). The crystalline size and d-spacing were calculated from the Scherrer formula and Bragg equation.

ATR FTIR spectra were recorded on the Thermo Scientific Nicolet iS50 spectrometer. Raman spectra were recorded in a Jasco/NRS-

3100 spectrophotometer. The crystallite size of Co@NC was calculated using Tuinstra–Koenig equation [50]:

$(L_a)_{nm} = 2.41 \times 10^{-10}\ x(\lambda_{nm})^4/(I_D/I_G)$ where

L_a = crystallite size, λ = the wavelength used for the measurement.

SEM studies were performed in a Hitachi S-2700 microscope. TEM studies were carried out in FEI Tecnai G^2 20 S-TWIN transmission electron microscope (FEI Company, Eindhoven, Netherlands) equipped with a LaB_6-source at 200 kV acceleration voltage. EDX analysis was carried out with an EDAX r-TEM SUTW Detector (Si (Li)-detector).

The XPS spectra were recorded in a Kratos Axis Ultra X-ray photoelectron spectrometer (Kratos Analytical Ltd., Manchester, UK) using Al K_α monochromatic radiation source (1,486.7 eV) with 90° take-off angle. XPS data fitting was done using Casa XPS (Casa Software Ltd.).

The surface area and pore size distribution were obtained by using Quantachrome Autosorb-1 apparatus. Barret-Joyner-Halenda method has been used to quantify BET surface area (S_{BET}) and pore size distribution by relating adsorption data of N_2 isotherm in relative to pressure range from 0.01 to 0.1.

The elemental analyses were performed on a Thermo Finnigan Flash EA 1112 Series instrument. The sample was prepared in silver capsule for measuring accurate measurements. The data were recorded thrice, and the average data were presented. The composition of the materials was evaluated by ICP-AES from Thermo Jarrell Ash Trace Scan analyzer.

Electrochemical measurements: All electrochemical measurements for OER calculation were measured by using a potentiostat (SP-200, BioLogic Science Instruments) controlled by EC-Lab v10.20 software package. The electrodes were prepared by EPD method by applying a potential difference of 10 V between anode and cathode in a solution of iodine (for 50 mg of catalyst, 3 mg of iodine) and acetone (10 mL) on 1 × 1 cm^2 area nickel foam (NF, Racemate BV). The catalytic activity of the catalyst was carried out in 1 M aqueous KOH solution at room temperature using a single-compartment three-electrode cell (material loaded on NF as a working electrode, Pt wire as a counter electrode, and Hg/HgO reference electrode).

Cyclic voltammetry (CV) and LSV were performed with 50% *iR* compensation. The potentials presented in this work were referenced to the RHE through RHE calibration, E (RHE) = E (Hg/HgO) + 0.098 V + (0.059 × pH) V [75]. Chronoamperometric measurement was performed in 1.0 M KOH solution at a constant potential (1.49 V vs. RHE).

The electrochemical double-layer capacitance, C_{dl}, was measured from CV curves recorded in a potential range with no Faradaic current at different scan rates from 10 to 200 mV/s (cycled between 0.90 and 1.00 V vs. RHE). The anodic charging currents were plotted as a function of the scan rate and from the, slope C_{dl}, was obtained.

Electrochemical impedance spectroscopy was performed at 1.55 V vs. RHE to obtain the Nyquist plots. The amplitude of the sinusoidal wave was surveyed in a frequency range of 100 kHz to 1 MHz. The impedance spectra were fitted using an equivalent R_C circuit model. The charge transfer resistance (R_{ct}) was then calculated from the diameter of the semicircle in the Nyquist plots.

The number of active sites for Co@NC during electrochemical water oxidation was calculated considering single-electron oxidation of Co^{II} to Co^{III} species [76–78]. The area associated with the oxidation peak was calculated to be 0.058×10^{-3} V A.

Hence, the associated charge = 0.058×10^{-3} V A/0.005 V/s = 11.600×10^{-3} C.

Now, the number of transferred electrons = 11.600×10^{-3} C/1.602×10^{-19} C = 7.240×10^{16}.

Therefore, the number of surface active sites that participated in OER = 7.240×10^{16}.

$TOF = (j \times N_A \times A)/(4 \times F \times n)$

where j = Current density = 0.1 A/cm^2; N_A = Avogadro number = 6.023×10^{23}; A = geometrical surface area = 1 cm^2; F = Faraday constant = 96,485 C/mol; n = number of surface active Co-sites for OER = 7.240×10^{16}.

The calculated TOF for Co@NC is 2.15 per second.

Authors' contributions

A.K.S. was involved in the synthesis, characterization, and electrochemical measurements. The density functional theory (DFT) calculations were performed by S.J. B.S. carried out the electrochemical measurements. XPS spectra measurements were done by C.D. H.C. interpreted the DFT result and wrote the article. P.W.M. was involved in data interpretation and editing of the article. The planning and designing of the project and writing of the article were performed by A.I.

Declaration of competing interest

The authors declare that they have no known competing financial interests or personal relationships that could have appeared to influence the work reported in this paper.

Acknowledgments

This work was financially supported by CSIR Grant no. 01(2977)/19/EMR-II), Govt. of India. B.S. acknowledges the research fellowship from DST-INSPIRE (180147). H.C. and S.J. acknowledge the financial support from the Federal Ministry of Education and Research under the "Make Our Planet Great Again-German Research Initiative" (MOPGA-GRI; 57429784) implemented by the German Academic Exchange Service: Deutscher Akademischer Austauschdienst (DAAD). P.W.M. acknowledges support from the German Federal Ministry of Education and Research in the framework of the project Catlab (03EW0015A/B).

Appendix A. Supplementary data

Supplementary data to this article can be found online at https://doi.org/10.1016/j.mtchem.2021.100668.

References

[1] Z.N. Zahran, E.A. Mohamed, Y. Tsubonouchi, M. Ishizaki, T. Togashi, M. Kurihara, K. Saito, T. Yui, M. Yagi, Electrocatalytic water splitting with unprecedentedly low overpotentials by Nickel sulfide nanowires stuffed into carbon nitride scabbards, Energy Environ. Sci. 14 (2021) 5358–5365, https://doi.org/10.1039/d1ee00509j.

[2] B. Singh, A. Indra, Prussian blue- and prussian blue analogue-derived materials: progress and prospects for electrochemical energy conversion, Mater. Today Energy 16 (2020) 100404.

[3] J. Sun, M. Ren, L. Yu, Z. Yang, L. Xie, F. Tian, Y. Yu, Z. Ren, S. Chen, H. Zhou, Highly efficient hydrogen evolution from a mesoporous hybrid of Nickel phosphide nanoparticles anchored on cobalt phosphosulfide/phosphide nanosheet arrays, Small 15 (2019) 1804272.

[4] A. Indra, T. Song, U. Paik, Metal organic framework derived materials: progress and prospects for the energy conversion and storage, Adv. Mater. 30 (2018) 1705146.

[5] B. Singh, A. Indra, Designing self-supported metal-organic framework derived catalysts for electrochemical water splitting, Chem. Asian J. 15 (2020) 607–623.

[6] S. Dutta, Z. Liu, H. Han, A. Indra, T. Song, Electrochemical energy conversion and storage with zeolitic imidazolate framework derived materials: a perspective, ChemElectroChem 5 (2018) 3571–3588.
[7] A. Indra, P.W. Menezes, M. Driess, Photocatalytic and Photosensitized Water Splitting: a plea for well-defined and commonly accepted protocol, C. R. Chim. 21 (2018) 909–915.
[8] F. Cai, L. Liao, Y. Zhao, D. Li, J. Zeng, F. Yu, H. Zhou, Large-current-stable bifunctional nanoporous Fe-rich nitride electrocatalysts for highly efficient overall water and urea splitting, J. Mater. Chem. 9 (2021) 10199–10207.
[9] F. Yu, L. Yu, I.K. Mishra, Y. Yu, Z.F. Ren, H.Q. Zhou, Recent developments in earth-abundant and non-noble electrocatalysts for water electrolysis, mater, Today Phys 7 (2018) 121–138.
[10] F. Yu, H. Zhou, Y. Huang, J. Sun, F. Qin, J. Bao, W.A. Goddard, S. Chen, Z. Ren, High-performance bifunctional porous non-noble metal phosphide catalyst for overall water splitting, Nat. Commun. 9 (2018) 2551.
[11] J. Balamurugan, T.T. Nguyen, V. Aravindan, N.H. Kim, J.H. Lee, Highly reversible water splitting cell building from hierarchical 3D Nickel manganese oxyphosphide nanosheets, Nanomater. Energy 69 (2020) 104432.
[12] J. Song, C. Wei, Z.F. Huang, C. Liu, L. Zeng, X. Wang, Z.J. Xu, A review on fundamentals for designing oxygen evolution electrocatalysts, Chem. Soc. Rev. 49 (2020) 2196–2214.
[13] X. Ji, K. Wang, Y. Zhang, H. Sun, Y. Zhang, T. Ma, Z. Ma, P. Hu, Y. Qiu, MoC based Mott–Schottky electrocatalyst for boosting the hydrogen evolution reaction performance, Sustain. Energy Fuels 4 (2020) 407–416.
[14] Z.H. Xue, H. Su, Q.Y. Yu, B. Zhang, H.H. Wang, X.H. Li, J.S. Chen, Janus Co/CoP nanoparticles as efficient Mott–Schottky electrocatalysts for overall water splitting in wide pH range, Adv. Energy Mater. 12 (2017) 1602355.
[15] X.H. Li, M. Antonietti, Metal nanoparticles at mesoporous N-doped carbons and carbon nitrides: functional Mott–Schottky heterojunctions for catalysis, Chem. Soc. Rev. 42 (2013) 6593–6604.
[16] X.H. Li, X.C. Wang, M. Antonietti, Mesoporous g-C_3N_4 nanorods as multifunctional supports of ultrafine metal nanoparticles: hydrogen generation from water and reduction of nitrophenol with tandem catalysis in one step, Chem. Sci. 3 (2012) 2170–2174.
[17] H. Su, K.X. Zhang, B. Zhang, H.H. Wang, Q.Y. Yu, X.H. Li, M. Antonietti, J.S. Chen, Activating cobalt nanoparticles via the Mott–Schottky effect in nitrogen-rich carbon shells for base-free aerobic oxidation of alcohols to esters, J. Am. Chem. Soc. 139 (2017) 811–818.
[18] B. Goel, V. Vyas, N. Tripathi, A.K. Singh, P.W. Menezes, A. Indra, S.K. Jain, Amidation of aldehydes with amines under mild conditions using metal-organic framework derived NiO@Ni Mott-Schottky catalyst, ChemCatChem 12 (2020) 5743–5749.
[19] A. Bähr, G.H. Moon, H. Tüysüz, Nitrogen-doped mesostructured carbon-supported metallic cobalt nanoparticles for oxygen evolution reaction, ACS Appl. Energy Mater. 2 (2019) 6672–6680.
[20] H. Guo, Q. Feng, J. Zhu, J. Xu, Q. Li, S. Liu, K. Xu, C. Zhang, T. Liu, Cobalt nanoparticle-embedded nitrogen-doped carbon/carbon nanotube frameworks derived from a metal–organic framework for tri-functional ORR, OER and HER electrocatalysis, J. Mater. Chem. 7 (2019) 3664–3672.
[21] S. Dutta, A. Indra, H.S. Han, T. Song, An intriguing pea-like nanostructure of cobalt phosphide on molybdenum carbide incorporated nitrogen-doped carbon nanosheets for efficient electrochemical water splitting, ChemSusChem 11 (2018) 3956–3964.
[22] C. Wang, L. Qiao, C.Q. Qu, W.T. Zheng, Q. First-principles calculations on the emission properties of pristine and N-doped carbon nanotubes, J. Jiang, Phys. Chem. C 113 (2009) 812–818.
[23] X.R. Wang, X.L. Li, L. Zhang, Y. Yoon, P.K. Weber, H.L. Wang, J. Guo, H.J. Dai, N-doping of graphene through electrothermal reactions with ammonia, Science 44 (2009) 324 768–771.
[24] J. Balamurugan, T.T. Nguyen, N.H. Kim, D.H. Kim, Joong HeeLee, Novel core-shell CuMo-oxynitride@N-doped graphene nanohybrid as multifunctional catalysts for rechargeable zinc-air batteries and water splitting, Nanomater. Energy 85 (2021) 105987.
[25] T.T. Nguyen, J. Balamurugan, K.T. Lau, N.H. Kim, J.H. Lee, Novel cobalt-doped molybdenum oxynitride quantum dot@N-doped carbon nanosheets with abundant oxygen vacancies for long-life rechargeable zinc–air batteries, J. Mater. Chem. 9 (2021) 9092–9104.
[26] D. Yu, P. RobertIlango, S. Han, M. Ye, Y. Hu, L. Li, S. Peng, Metal-organic framework derived Co@NC/CNT hybrid as a multifunctional electrocatalyst for hydrogen and oxygen evolution reaction and oxygen reduction reaction, Int. J. Hydrogen Energy 44 (2019) 32054–32065.
[27] J. Chen, Y. Zhang, H. Ye, J.Q. Xie, Y. Li, C. Yan, R. Sun, C.P. Wong, Metal–organic framework-derived CoxFe1−xP nanoparticles encapsulated in N-doped carbon as efficient bifunctional electrocatalysts for overall water splitting, ACS Appl. Energy Mater. 2 (2019) 2734–2742.
[28] X. Wu, S. Han, D. He, C. Yu, C. Lei, W. Liu, G. Zheng, X. Zhang, L. Lei, Metal organic framework derived Fe-doped CoSe2 incorporated in nitrogen-doped carbon hybrid for efficient hydrogen evolution, ACS Sustain. Chem. Eng. 6 (2018) 8672–8678.
[29] L. Han, T. Yu, W. Lei, W. Liu, K. Feng, Y. Ding, G. Jiang, P. Xu, Z. Chen, Nitrogen-doped carbon nanocones encapsulating with nickel–cobalt mixed phosphides for enhanced hydrogen evolution reaction, J. Mater. Chem. 5 (2017) 16568–16572.
[30] P. Jiang, J. Chen, C. Wang, K. Yang, S. Gong, S. Liu, Z. Lin, M. Li, G. Xia, Y. Yang, J. Su, Q. Chen, Tuning the activity of carbon for electrocatalytic hydrogen evolution via an iridium-cobalt alloy core encapsulated in nitrogen-doped carbon cages, Adv. Mater. 30 (2018) 1705324.
[31] Q. Hu, X. Liu, C. Tang, L. Fan, X. Chai, Q. Zhang, J. Liu, C. He, Facile fabrication of a 3D network composed of N-doped carbon-coated core–shell metal oxides/phosphides for highly efficient water splitting, Sustain. Energy Fuels 2 (2018) 1085–1092.
[32] Y. Pan, K. Sun, S. Liu, X. Cao, K. Wu, W.C. Cheong, Z. Chen, Y. Wang, Y. Li, Y. Liu, D. Wang, Q. Peng, C. Chen, Y. Li, Core–shell ZIF-8@ZIF-67-derived CoP nanoparticle-embedded N-doped carbon nanotube hollow polyhedron for efficient overall water splitting, J. Am. Chem. Soc. 140 (2018) 2610–2618.
[33] C.C. Yang, S.F. Zai, Y.T. Zhou, L. Du, Q. Jiang, Fe_3C-Co nanoparticles encapsulated in a hierarchical structure of N-doped carbon as a multifunctional electrocatalyst for ORR, OER, and HER, Adv. Funct. Mater. 29 (2019) 1901949.
[34] J. Hou, Y. Sun, Y. Wu, S. Cao, L. Sun, Promoting active sites in core–shell nanowire array as Mott–Schottky electrocatalysts for efficient and stable overall water splitting, Adv. Funct. Mater. 28 (2018) 1704447.
[35] X. Gao, L. Mei, Y. Zhou, Z. Shen, Impact of electron transfer of atomic metals on adjacent graphyne layers on electrochemical water splitting, Nanoscale 12 (2020) 7814–7821.
[36] Y. Feng, X.Y. Yu, U. Paik, N-doped graphene layers encapsulated NiFe alloy nanoparticles derived from MOFs with superior electrochemical performance for oxygen evolution reaction, Sci. Rep. 6 (2016) 34004.
[37] A. Sivanantham, P. Ganesan, L. Estevez, B.P. McGrail, R.K. Motkuri, S. Shanmugam, A stable graphitic, nanocarbon-encapsulated, cobalt-rich core–shell electrocatalyst as an oxygen electrode in a water electrolyzer, Adv. Energy Mater. 8 (2018) 1702838.
[38] D. Lyu, Y. Du, S. Huang, B.Y. Mollamahale, X. Zhang, S.W. Hasan, F. Yu, S. Wang, Z.Q. Tian, P.K. Shen, Highly efficient multifunctional Co–N–C electrocatalysts with synergistic effects of Co–N moieties and Co metallic nanoparticles encapsulated in a N-doped carbon matrix for water-splitting and oxygen redox reactions, ACS Appl. Mater. Interfaces 11 (2019) 39809–39819.
[39] F. Yang, P. Zhao, X. Hua, W. Luo, G. Cheng, W. Xing, S. Chen, A cobalt-based hybrid electrocatalyst derived from a carbon nanotube inserted metal–organic framework for efficient water-splitting, J. Mater. Chem. 4 (2016) 16057–16063.
[40] X. Liu, X. Zhao, Z. Fan, Boosting oxygen evolution reaction activity by tailoring MOF-derived hierarchical Co–Ni alloy nanoparticles encapsulated in nitrogen-doped carbon frameworks, RSC Adv. 11 (2021) 10874–10880.
[41] C. Wang, Y. Wang, H. Yang, Y. Zhang, H. Zhao, Q. Wang, Revealing the role of electrocatalyst crystal structure on oxygen evolution reaction with Nickel as an example, Small 14 (2018) 1802895.
[42] Y. Wang, C. An, Y. Wang, Y. Huang, C. Chen, L. Jiao, H. Yuan, Core–shell Co@C catalyzed MgH_2: enhanced dehydrogenation properties and its catalytic mechanism, J. Mater. Chem. 2 (2014) 16285–16291.
[43] M. Zhang, Q. Dai, H. Zheng, M. Chen, L. Dai, Novel MOF-derived Co@N-C bifunctional catalysts for highly efficient Zn–air batteries and water splitting, Adv. Mater. 30 (2018) 1705431.
[44] L. Meziane, C. Salzemann, C. Aubert, H. Gérard, C. Petit, M. Petit, Hcp cobalt nanocrystals with high magnetic anisotropy prepared by easy one-pot synthesis, Nanoscale 8 (2016) 18640–18645.
[45] K.M. Nam, J.H. Shim, H. Ki, S. Choi, G. Lee, J.K. Jang, Y. Jo, M. Jung, H. Song, J.T. Park, Single-crystalline hollow face-centered-cubic cobalt nanoparticles from solid face-centered-cubic cobalt oxide nanoparticles, Angew. Chem. Int. Ed. 47 (2008) 9504–9508.
[46] J. Su, Y. Yang, G. Xia, J. Chen, P. Jiang, Q. Chen, Ruthenium-cobalt nanoalloys encapsulated in nitrogen-doped graphene as active electrocatalysts for producing hydrogen in alkaline media, Nat. Commun. 8 (2017) 14969.
[47] Y. Yang, Z. Lun, G. Xia, F. Zheng, M. He, Q. Chen, Non-precious alloy encapsulated in nitrogen-doped graphene layers derived from MOFs as an active and durable hydrogen evolution reaction catalyst, Energy Environ. Sci. 8 (2015) 3563–3571.
[48] C. Ferrari, D.M. Basko, Raman spectroscopy as a versatile tool for studying the properties of graphene, Nat. Nanotechnol. 8 (2013) 235–246.
[49] V. Kumar, A. Kumar, D.J. Lee, S.S. Park, Estimation of number of graphene layers using different methods: a focused review, Materials 14 (2021) 4590.
[50] A. Kołodziej, E. Długon, M. Swietek, M. Ziabka, E. Dawiec, M. Gubernat, M. Michalec, A.W. Birczynska, Raman spectroscopic analysis of polymer membranes with graphene oxide and reduced graphene oxide, J. Compos. Sci. 5 (2021) 20.
[51] J. Lu, Y. Zeng, X. Ma, H. Wang, L. Gao, H. Zhong, Q. Meng, Cobalt nanoparticles embedded into N-doped carbon from metal organic frameworks as highly active electrocatalyst for oxygen evolution reaction, Polymers 11 (2019) 828.
[52] Y. Li, F. Cheng, J. Zhang, Z. Chen, Q. Xu, S. Guo, Cobalt-carbon core–shell nanoparticles aligned on wrinkle of N-doped carbon nanosheets with Pt-like activity for oxygen reduction, Small 12 (2016) 2839–2845.
[53] B. Pan, X. Peng, Y. Wang, Q. An, X. Zhang, Y. Zhang, Tracking the pyrolysis process of a 3-MeOsalophen-ligand based Co_2 complex for promoted oxygen evolution reaction, Chem. Sci. 10 (2019) 4560–4566.
[54] B. Kumar, M. Asadi, D. Pisasale, S.S. Ray, B.A. Rosen, R. Haasch, J. Abiade, A.L. Yarin, A.S. Khojin, Renewable and metal-free carbon nanofibre catalysts for carbon dioxide reduction, Nat. Commun. 4 (2013) 2819.
[55] Y. Jiang, K. Dong, X. Yan, C. Chen, P. Ni, C. Yang, Y. Lu, Metal–polydopamine framework-derived (Co)/N-doped carbon hollow nanocubes as efficient oxygen electrocatalysts, Sustain. Energy Fuels 4 (2020) 3370–3377.

[56] S.W. Lee, N. Yabuuchi, B.M. Gallant, S. Chen, B.S. Kim, P.T. Hammond, Y.S. Horn, High-power lithium batteries from functionalized carbon-nanotube electrodes, Nat. Nanotechnol. 5 (2010) 531–537.
[57] D. Yang, A. Velamakanni, G. Bozoklu, S. Park, M. Stoller, R.D. Piner, S. Stankovich, I. Jung, D.A. Field, C.A. Ventrice Jr., R.S. Ruoffa, Chemical analysis of graphene oxide films after heat and chemical treatments by X-ray photoelectron and micro-Raman spectroscopy, Carbon 47 (2009) 145–152.
[58] Y. Xie, P.M.A. Sherwood, X-ray photoelectron-spectroscopic studies of carbon fiber surfaces. 11. Differences in the surface chemistry and bulk structure of different carbon fibers based on poly(acrylonitrile) and pitch and comparison with various graphite samples, Chem. Mater. 2 (1990) 293–299.
[59] P.W. Menezes, C. Panda, S. Garai, C. Walter, A. Guiet, M. Driess, Structurally ordered intermetallic cobalt stannide nanocrystals for high-performance electrocatalytic overall water-splitting, Angew. Chem. Int. Ed. 130 (2018) 15457–15462.
[60] A. Indra, P.W. Menezes, I. Zaharieva, H. Dau, M. Driess, Detecting structural transformation of cobalt phosphonate to active bifunctional catalysts for electrochemical water-splitting, J. Mater. Chem. 8 (2020) 2637–2643.
[61] B. Singh, O. Prakash, P. Maiti, P.W. Menezes, A. Indra, Electrochemical transformation of Prussian blue analogues into ultrathin layered double hydroxide nanosheets for water splitting, Chem. Commun. 56 (2020) 15036.
[62] B. Singh, O. Prakash, P. Maiti, A. Indra, Electrochemical transformation of metal organic framework into ultrathin metal hydroxide-(oxy)hydroxide nanosheets for alkaline water oxidation, ACS Appl. Nano Mater. 3 (2020) 6693–6701.
[63] A. Indra, U. Paik, T. Song, Boosting electrochemical water oxidation with metal hydroxide carbonate templated prussian blue analogues, Angew. Chem. Int. Ed. 57 (2018) 1241–1245.
[64] A. Indra, P.W. Menezes, C. Das, C. Göbel, D. Schmeißer, M. Driess, Alkaline electrochemical water oxidation with multi-shelled cobalt manganese oxide hollow spheres, Chem. Commun. 53 (2017) 8641–8644.
[65] P.W. Menezes, A. Indra, I. Zaharieva, C. Walter, S. Loos, S. Hoffmann, R. Schlögl, H. Dau, M. Driess, Helical cobalt borophosphates to master durable overall water-splitting, Energy Environ. Sci. 12 (2019) 988–999.
[66] S.W. Lee, N. Yabuuchi, B.M. Gallant, S. Chen, B.S. Kim, P.T. Hammond, Y.S. Horn, High-power lithium batteries from functionalized carbon-nanotube electrodes, Nat. Nanotechnol. 5 (2010) 531–537.
[67] Reikowski, F. Maroun, I. Pacheco, T. Wiegmann, P. Allongue, J. Stettner, O.M. Magnussen, Operando Surface X-ray Diffraction Studies of Structurally Defined Co3O4 and CoOOH Thin Films during Oxygen Evolution, ACS Catal. 9 (2019) 3811–3821.
[68] T.T. Nguyen, J. Balamurugan, D.H. Kim, N.H. Kim, Joong Hee Lee, Hierarchical 3D oxygenated cobalt vanadium selenide nanosheets as advanced electrode for flexible zinc–cobalt and zinc–air batteries, Small 16 (2020) 2004661.
[69] S.R. Carbonell, K. Artyushkova, A. Serov, C. Santoro, I. Matanovic, P. Atanassov, Effect of pH on the activity of platinum group metal-free catalysts in oxygen reduction reaction, ACS Catal. 8 (2018) 3041–3053.
[70] L.M.R. Keil, F.M. Möller, M. Kieß, P.W. Kudella, C.B. Mast, Proton gradients and pH oscillations emerge from heat flow at the microscale, Nat. Commun. 8 (2017) 1–9.
[71] H. Dau, C. Pasquini, Modelling the (essential) role of proton transport by electrolyte bases for electrochemical water oxidation at near-neutral pH, Inorganics 7 (2019) 20.
[72] M. Sharma, J.H. Jang, D.Y. Shin, J.A. Kwon, D.H. Lim, D. Choi, H. Sung, J. Jang, S.Y. Lee, K.Y. Lee, H.Y. Park, N. Jung, S.J. Yoo, Work function-tailored graphene via transition metal encapsulation as a highly active and durable catalyst for the oxygen reduction reaction, Energy Environ. Sci. 12 (2019) 2200–2211.
[73] T. Cusati, G. Fiori, A. Gahoi, V. Passi, M.C. Lemme, A. Fortunelli, G. Iannaccone, Electrical properties of graphene-metal contacts, Sci. Rep. 7 (2017) 1–11.
[74] B. Wang, K. Chen, G. Wang, X. Liu, H. Wang, J. Bai, A multidimensional and hierarchical carbon-confined cobalt phosphide nanocomposite as an advanced anode for lithium and sodium storage, Nanoscale 11 (2019) 968–985.
[75] J. Zhu, D. Xu, C. Wang, W. Qian, J. Guo, F. Yan, Ferric citrate-derived N-doped hierarchical porous carbons for oxygen reduction reaction and electrochemical supercapacitors, Carbon 115 (2017) 1–10.
[76] B. Singh, A. Indra, Tuning the properties of CoFe-layered double hydroxide by vanadium substitution for improved water splitting activity, Dalton Trans. 50 (2021) 2359–2363.
[77] M. Łukaszewski, M. Soszko, A. Czerwiński, Electrochemical methods of real surface area determination of noble metal electrodes – an overview, Int. J. Electrochem. Sci. 11 (2016) 4442–4469.
[78] S. Anantharaj, P.E. Karthik, S. Noda, The significance of properly reporting turnover frequency in electrocatalysis research, Angew. Chem. Int. Ed. 60 (2021) 23051–23067, https://doi.org/10.1002/anie.202110352.